# Topological Nernst and topological thermal Hall effect in rare-earth kagome $ScMn_6Sn_6$

Richa P. Madhogaria,[1,*] Shirin Mozaffari,[1] Heda Zhang,[2] William R. Meier,[1] Seung-Hwan Do,[1] Rui Xue,[3] Takahiro Matsuoka,[1] and David G. Mandrus[1,2,3,†]

[1]*Department of Materials Sciences and Engineering, University of Tennessee, Knoxville, Tennessee 37996, USA*
[2]*Materials Science and Technology Division, Oak Ridge National Laboratory, Oak Ridge, Tennessee 37831, USA*
[3]*Department of Physics and Astronomy, University of Tennessee Knoxville, Knoxville, Tennessee 37996, USA*

(Received 16 June 2023; accepted 28 August 2023; published 7 September 2023)

Thermal and thermoelectric measurements are known as powerful tools to uncover the physical properties of quantum materials due to their sensitivity towards the scattering and chirality of heat carriers. We use these techniques to confirm the presence of momentum and real-space topology in $ScMn_6Sn_6$. There is an unconventional dramatic increase in the Seebeck coefficient on entering the transverse conical spiral (TCS) state below $T = 200$ K, suggesting an unusual scattering of heat carriers. In addition, the observed anomalous thermal Hall effect and the anomalous Nernst effect indicate nonzero Berry curvature in $k$ space. Furthermore, we identify a significant topological contribution to the thermal Hall and Nernst signals in the TCS phase revealing the impacts of real-space Berry curvature. We discuss the presence of the topological thermal Hall effect and topological Nernst effect in the diverse $HfFe_6Ge_6$ family. This study illustrates the importance of transverse thermal and thermoelectric measurements to investigate the origin of topological transport in the noncoplanar magnetic phases in this family of kagome metals.

DOI: 10.1103/PhysRevB.108.125114

## I. INTRODUCTION

Thermal and thermoelectric transport measurements are a powerful technique to help discover the intriguing physical properties of quantum materials [1–4]. Importantly, studying the thermal properties give insight into charge neutral excitations such as lattice vibrations (phonons), and magnons, which are not detected via electrical methods. These measurements are compelling for insulators to retrieve information regarding the dynamics of the charge neutral heat carriers and can be equally used for metallic systems [4–8]. The transverse thermal and thermoelectric counterparts of the electrical anomalous Hall effect (AHE), $\sigma^A_{xy}$, are the anomalous thermal Hall effect (ATHE), $\kappa^A_{xy}$, and the anomalous Nernst effect (ANE), $S^A_{xy}$, respectively. As a general rule, the Hall signal can be separated into three components based on their origin: ordinary contributions arising from the deflection of carriers by the applied field, anomalous contributions stemming from Berry curvature in $k$ space, and a topological contribution from real-space Berry curvature emerging from spin textures. Out of the three, the anomalous parts can be mathematically expressed as [3,9–12]

$$\sigma^A_{xy} = -2\pi e^2/h \int_{BZ} (d^3k)/(2\pi)^3 f(k)\Omega_B(k), \quad (1)$$

$$\kappa^A_{xy} = -2\pi/hT \int_{BZ} (d^3k)/(2\pi)^3 \epsilon f(k)\Omega_B(k), \quad (2)$$

$$\alpha^A_{xy} = -2\pi e^2/h \int_{BZ} (d^3k)/(2\pi)^3 \gamma(k)\Omega_B(k), \quad (3)$$

$$S_{xy} = \left(\sigma_{xx}\alpha^A_{xy} - \sigma^A_{xy}\alpha_{xx}\right), \quad (4)$$

where $\Omega_B(k)$ is the Berry phase curvature, $f(k)$ is the Fermi-Dirac distribution function, $\epsilon$ is the energy, $\alpha_{xy}$ is the transverse component of the thermoelectric tensor, and $\gamma(k) = -f(k)\ln[f(k)] - [1 - f(k)]\ln[1 - f(k)]$ [10]. From the mathematical formulation, it is clear that similar to AHE, both ATHE and ANE are also dependent on the Berry curvature (BC) of the electron bands and hence can serve as two other transport tools to probe the nontrivial BC. All three effects appear when the charge carriers acquire an anomalous transverse velocity and a finite Berry phase in the presence of longitudinal current or thermal gradient [1,2,9]. However, the three anomalous Hall transports provide access to BC with different weights; $f(k)$, $\epsilon f(k)$, and $\gamma(k)$ for $\sigma^A_{xy}$, $\kappa^A_{xy}$, and $S^A_{xy}$, respectively. As a consequence, $\kappa^A_{xy}$ and $S^A_{xy}$ provide additional information about the entropy and the velocities of the electrons near the Fermi surface.

The third component which is the manifestation of the spin textures, namely, the topological Hall effect (THE) (electrical), topological thermal Hall effect (TTHE) (thermal), and topological Nernst effect (TNE) (thermoelectric), are found to be superimposed on the anomalous signals and most of the time are very subtle to detect. Specifically, these effects have been assigned to the presence of nonzero static spin chirality generated due to the chiral (or noncoplanar) spin texture [8,13,14]. Although they share a common origin it is not yet well understood why all the materials that exhibit THE do not show TTHE and TNE.

*rpokhar1@utk.edu
†dmandrus@utk.edu

 

THE has been widely studied in different classes of materials, from manganites [15] to frustrated magnets [16] to the bulk skyrmions [13], whereas TNE and TTHE have been extremely difficult to observe in the experiments. While there is only one experimental report for TTHE ($GaV_4Se_8$) [14], a few materials are reported to host TNE, for example, $Fe_3Sn_2$ [8], MnGe [17], $Gd_2PdSi_3$ [18], $EuCd_2As_2$ [19], and $Nd_3Ru_4Al_{12}$ [2]. The scalar spin chirality coupled with the conduction electrons is responsible for the TNE. The first three aforementioned materials host skyrmions which generate scalar spin chirality, while the possibility of a nontrivial spin structure in the antiferromagnetic (AFM) phase of $EuCd_2As_2$ and spin canting due to the thermal fluctuations at the vicinity of the ferromagnetic ordering in $Nd_3Ru_4Al_{12}$ lead to the chiral magnetic state. The study on $EuCd_2As_2$ and $Nd_3Ru_4Al_{12}$ opens up a different perspective to explore the topological Nernst effect beyond skyrmionic systems. The lack of experiments to explore topological effects other than THE motivates us to investigate TTHE and TNE in $ScMn_6Sn_6$, a nonskyrmion system.

The diverse family of hexagonal $HfFe_6Ge_6$ materials provides a huge platform for additional phenomena owing to their exotic band structure, which includes Dirac points, van Hove singularities, flat bands, and their high tunability [20–24]. A room-temperature topological Hall effect in $YMn_6Sn_6$ [21], a Chern gap coupled with magnetism and a skyrmion spin lattice in $TbMn_6Sn_6$ [22], quantum oscillations from the nontrivial Berry phase in $RMn_6Sn_6$ ($R$ = Gd-Tm, Lu) [25], an exotic phonon-driven charge density wave in $ScV_6Sn_6$ [24,26,27], and $Z_2$ topological kagome metals [28] are some of the examples which necessitate the study of this class of materials.

Figure 1(a) (top) shows the schematic crystal structure of $ScMn_6Sn_6$. In this material, Mn atoms form double-layered kagome sheets which are represented by the blue atoms in the figure. The magnetic spins align ferromagnetically within the kagome sheets and are helically coupled along the $c$ axis [29]. $ScMn_6Sn_6$ orders antiferromagnetically below $T_N = 390$ K [Fig. 1(b)] and transitions through multiple magnetic phases as the strength of the external magnetic field is increased [Fig. 1(c)]. As can be seen from Fig. 1(c), the magnetic structure evolves from a double spiral (DS) to a transverse conical spiral (TCS) to a fanlike (FL) and finally to a forced ferromagnetic (FFM) state at high magnetic field [29]. These phases of $ScMn_6Sn_6$ are very similar to the one reported for $YMn_6Sn_6$ [21]. A small-angle neutron scattering study on $YMn_6Sn_6$ shows the absence of a skyrmion lattice in the TCS phase [30]. Since the magnetism in $ScMn_6Sn_6$ is closely associated with $YMn_6Sn_6$, $ScMn_6Sn_6$ is considered to be a nonskyrmionic candidate.

In this paper we focus on understanding how the presence of exotic magnetic phases can affect its transport properties. Here, we report a comprehensive thermal and thermoelectric transport study on the kagome metal $ScMn_6Sn_6$. Both ATHE and ANE appear at $T = 300$ K and persist down to the lowest measured temperature, $T = 120$ K. The presence of ATHE and ANE manifest the existence of a large Berry curvature in $ScMn_6Sn_6$. A large anomalous Nernst signal, 2.21 $\mu V\,K^{-1}$, is seen at room temperature which is similar to that reported for the sister compounds $YMn_6Sn_6$ [31] and $TbMn_6Sn_6$ [32,33],

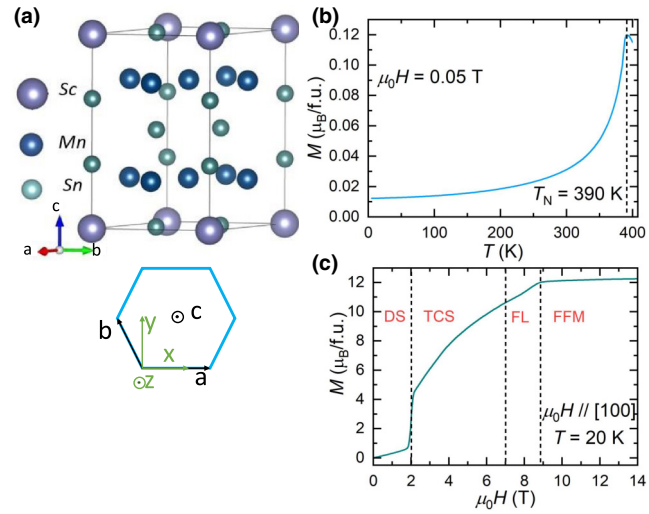


FIG. 1. (a) Schematic crystal structure of $ScMn_6Sn_6$: The formation of kagome layers by Mn atoms (blue spheres) can be clearly seen in the top panel; the bottom panel illustrates the crystal axes and the coordinate axes of a hexagonal-shaped crystal. (b) Temperature dependence of zero-field-cooled magnetization ($M$) curve at 0.05 T. (c) Field-dependent magnetization at $T = 20$ K. For both the magnetization curves the external magnetic field was parallel to [100]. The evolution of different magnetic phases, a double spiral (DS) to transverse conical spiral (TCS) to fanlike (FL) to forced ferromagnetic (FFM), can be seen from the $M$ vs $\mu_0H$ graph.

and comparable to the highest ANE observed [11]. In addition to the ATHE and ANE, $ScMn_6Sn_6$ also exhibits TNE from $T = 120$ to 300 K and TTHE from $T = 120$ to 280 K within the field regime $\mu_0H = 1.6$–5.3 T. The width of the magnetic field which shows the TNE and TTHE corresponds to the TCS magnetic phase of $ScMn_6Sn_6$, revealing a close association between the noncoplanar TCS phase (real-space topology) and the topological effects. Our results establish the importance of the thermal/thermoelectric measurements to reveal the inherent topology of the quantum materials.

## II. EXPERIMENTS

*Growth and characterization*. Single crystals of $ScMn_6Sn_6$ were grown via the self-flux method. Sc (Alfa Aesar 99.9%) and Mn (Alfa Aesar 99.98%) pieces were combined with a Sn shot (Alfa Aesar 99.999%) in an atomic ratio of Sc : Mn : Sn = 1 : 6 : 30 in a Canfield crucible set [34]. The crucible was then sealed in a silica tube under vacuum. The ampule was heated at 60 °C $h^{-1}$ to 973 °C, followed by a 48-h dwell. Crystals were grown during slow cool (1.2 °C $h^{-1}$) to 600 °C. The hexagonal-shaped $ScMn_6Sn_6$ crystals were retrieved from the molten Sn flux by centrifuging. The $HfFe_6Ge_6$-type structure was confirmed through powder x-ray diffraction (PXRD) using a PANalytical Empyrean diffractometer with a Cu $K\alpha$ source. The chemical composition and homogeneity of the crystals were confirmed through energy-dispersive x-ray spectroscopy. FULLPROF was used for the Reitveld refinement of the room-temperature PXRD data (Supplemental Fig. S1 [35]) and the obtained lattice parameters were $a = 5.464\,93(4)$ Å and $c = 8.960\,77(4)$ Å.

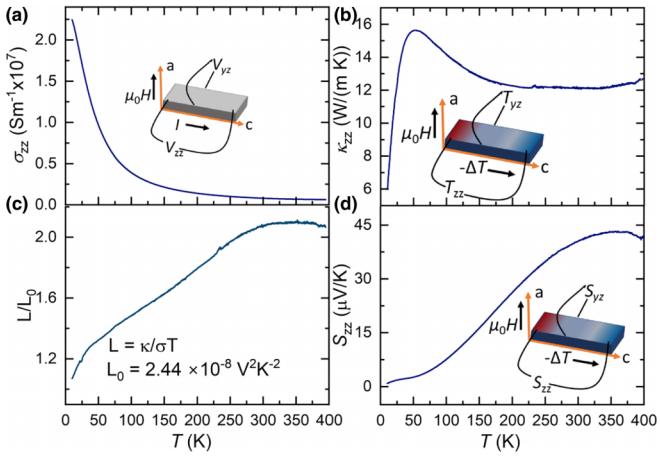


FIG. 2. Temperature dependence of electrical and thermal measurements. (a) Electrical conductivity vs temperature and (b) thermal conductivity vs temperature. (c) Deviation of the Lorenz number from the expected theoretical value with respect to the temperature. (d) Temperature dependence of the Seebeck coefficient. The direction of the applied magnetic field and current/temperature gradient are shown in the insets of (a), (b), and (d). The color gradient represents the flow of heat from the hot to cold end.

*Magnetization measurements*. Magnetization measurements were carried out using the vibrating sample magnetometer (VSM) option of a physical property measurement system (PPMS) from Quantum Design.

*Transport measurements*. Single crystals were shaped into a rectangular bar such that the external applied magnetic field is parallel to [100] and the current/temperature gradient is parallel to the [001] crystallographic axes. The electrical measurements were done using the resistivity option of the PPMS. The thermoelectric measurements were performed using a PPMS compatible self-designed sample puck and a break-out box. Type E chromel-constantan thermocouples were used to measure the temperature gradient. The schematic of the device is shown in Fig. S2 of the Supplemental Material [35]. The temperature gradient over the sample was created by attaching one end to the heater with 1 kΩ resistance and the other end to a piece of copper. A Keithley current source 2450 was used for applying the current and Keithley 2182A nanovoltmeters were used to record the induced voltage. The longitudinal thermal resistivity (anomalous thermal Hall resistivity) was obtained by symmetrizing (antisymmetrizing) the measured temperature gradient in the presence of a positive and negative magnetic field separately. Similarly, Seebeck and Nernst signals were also acquired through symmetrized and antisymmetrized thermoelectric voltages, respectively. The signs of the transverse components are explained in the Supplemental Material [35].

## III. RESULTS AND DISCUSSIONS

We present the bulk electronic and thermal properties of $ScMn_6Sn_6$. The temperature dependence of electrical conductivity ($\sigma_{zz}$), thermal conductivity ($\kappa_{zz}$), and the Seebeck coefficient ($S_{zz}$) of $ScMn_6Sn_6$ are shown in Figs. 2(a), 2(b), and 2(d), respectively. The insets of these figures represent the geometry of the experiments used for this study. For electrical measurements as shown in the inset of Fig. 2(a), the applied current is parallel to the $z$ axis, the magnetic field is along the $x$ axis, and the transverse voltage is parallel to the $y$ axis. Similarly, for the thermal and thermoelectric measurements the insets of Figs. 2(b) and 2(d) show the direction of the applied temperature gradient (|| $z$ axis), magnetic field (|| $x$ axis), and transverse temperature gradient/thermoelectric voltage (|| $y$ axis). [Note: Refer to the bottom image of Fig. 1(a) for the crystallographic and coordinate axes of hexagonal-shaped crystals.] The temperature-dependent $\sigma_{zz}$ decreases monotonically [Fig. 2(a)] as we warm up from $T = 2$ to 400 K, indicating the metallic nature of the sample. The temperature profile of $\kappa_{zz}$ [Fig. 2(b)] reflects a similar trend of the thermal conductivity as expected by the Debye approximation. As the temperature is raised from $T = 2$ to 400 K, it shows an increase, with a broad characteristic peak at $T =$ 52.5 K, and then a decrease followed with an almost saturated value above $T = 200$ K. The peak at $T = 52.5$ K corresponds to the competition between two phonon scattering mechanisms: low temperature, where the phonon scattering is dominated by the defects/boundary, and high temperature, where this process is governed by the umklapp phonon scattering [36]. The Wiedemann-Franz law, $L = (\frac{\kappa}{T\sigma})$, states that the ratio of thermal conductivity to the electrical conductivity is temperature independent and can be represented in terms of the Lorenz number for a metallic system. Nevertheless, as shown in Fig. 2(c), this number varies with temperature for $ScMn_6Sn_6$. This variation from the required value of $L_0 = 2.44 \times 10^{-8}$ V$^2$ K$^{-2}$ is suggestive of inelastic phonon scattering [37,38].

Figure 2(d) displays the temperature-dependent profile for $S_{zz}$. The Seebeck coefficient is defined as $S_{zz} = -\partial_z U/\partial_z T$, where $U$ is the longitudinal thermoelectric voltage and $T$ is the measured temperature. Alternatively, $S_{zz}$ can also be understood as an averaged entropy flow per charge carrier [39]. It can be seen that the magnitude of $S_{zz}$ increases constantly with an increase in temperature and remains positive throughout the measured temperature regime [Fig. 2(d)]. The positive value of $S_{zz}$ can be associated with the predominant $p$-type charge carriers present in the system. Moreover, it has a high magnitude of 40 μV K$^{-1}$ at $T = 300$ K. To understand what this means, let us look at the Seebeck coefficient based on the Mott relation [40,41],

$$S = -\frac{\pi^2 k_B^2 T}{3e}\left[\frac{\partial \ln D(\epsilon)}{\partial \epsilon} + \frac{\partial \ln \tau(\epsilon)}{\partial \epsilon}\right]_{\epsilon=\epsilon_F}, \qquad (5)$$

where $k_B$, $e$, $D(\epsilon)$, $\tau(\epsilon)$, and $\epsilon_F$ are the Boltzmann constant, electronic charge, density of states, relaxation time, and Fermi energy, respectively. According to the above relation, for a metallic system $S$ is a few μV K$^{-1}$ owing to the symmetric band structure around the Fermi level which allows for the cancellation of entropy flow of electrons above and below the Fermi level, whereas an asymmetric band structure leading to an asymmetric density of states contributes to the higher value of $S$ [40,42]. Hence, we suspect that the magnitude of $S_{zz}$ at $T = 300$ K (40 μV K$^{-1}$) is due to the nontrivial electronic topology of $ScMn_6Sn_6$. The slight downturn seen

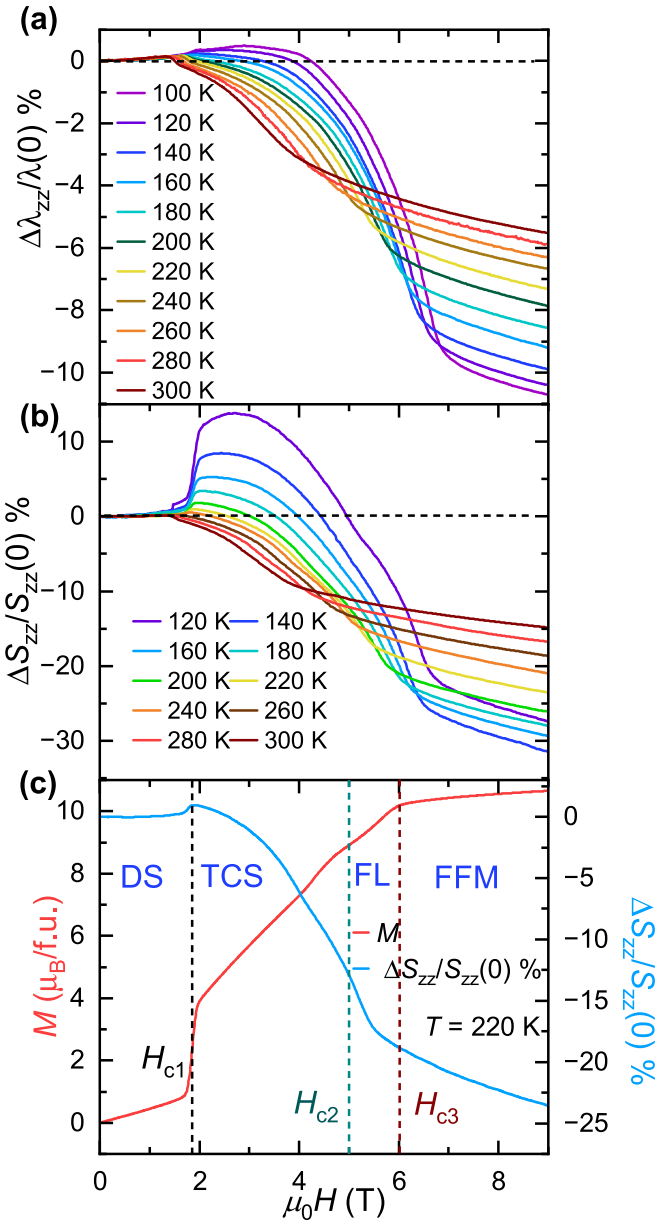


FIG. 3. The magnetic field dependence of the change in the longitudinal thermal resistivity and change in the Seebeck coefficient for various temperatures are shown in (a) and (b), respectively. (c) Comparison between the magnetization curve and change in Seebeck coefficient at $T = 220$ K are shown. Both curves go through a change in slope as the external applied field is increased, signifying the evolution of the magnetic structure: DS to TCS to FL to FFM in $ScMn_6Sn_6$.

in the data at $T = 374$ K could be due to the proximity of the antiferromagnetic transition.

Further, we investigate the effect of magnetic field on the longitudinal thermal and thermoelectric properties of $ScMn_6Sn_6$. Figures 3(a) and 3(b) show the magnetic field dependence of change in thermal resistivity [$\Delta\lambda_{zz}/\lambda_{zz}(0)$] and change in $S_{zz}$ for $\mu_0 H = 0 - 9$ T and $T = 100 - 300$ K. $\Delta\lambda_{zz}/\lambda_{zz}(0)$ manifests not only electrons, but also the charge neutral quasiparticle contributions such as phonons and magnons carrying heat. The change in $\Delta\lambda_{zz}/\lambda_{zz}(0)$ and $\Delta S_{zz}/S_{zz}(0)$ is almost negligible for $\mu_0 H < 2$ T, followed by two slope changes at critical fields $H_{c1}$ and $H_{c2}$ as we increase the magnetic field beyond 2 T before it saturates at fields higher than $H_{c3}$. $H_{c1}$, $H_{c2}$, and $H_{c3}$ are the critical fields corresponding to the magnetic phase transitions from DS-TCS, TCS-FL, and FL-FFM, respectively. The slope changes in $\Delta\lambda_{zz}/\lambda_{zz}(0)$ and $\Delta S_{zz}/S_{zz}(0)$ occur at the magnetic phase transitions which indicates the strong coupling between thermal/thermoelectric properties and magnetic structures. To show this relationship more clearly we compare between the magnetization and $\Delta S_{zz}/S_{zz}(0)$ curves at $T = 220$ K [Fig. 3(c)]. The dashed lines help to see the one-to-one correspondence between the slope changes of the magnetization and $\Delta S_{zz}/S_{zz}(0)$ curves. In the past, reports of similar studies on different magnetic materials with $\Delta S_{zz}/S_{zz}(0)$ showing an identical trend have also been linked with the presence of nontrivial magnetic textures [8,31,40,43]. According to the preliminary studies of the relationship between the Seebeck coefficient and magnetism, there are two representative mechanisms that explain the change in the slope of $\Delta S_{zz}/S_{zz}(0)$: (1) The alignment of the spins due to the external magnetic field reduces the spin scattering process which then affects the charge dynamics; and (2) as stated earlier, $S_{zz}$ can be explained in terms of the average entropy of the charge carriers. So the large entropy change that occurs during any magnetic phase evolution contributes to $\Delta S_{zz}/S_{zz}(0)$.

On closer inspection we see that for $T \leqslant 200$ K the percentage change of thermopower becomes positive within a certain field range in the TCS phase as $\mu_0 H$ is increased above $H_{c1}$. The strength of the non-negative signal becomes stronger as the system is cooled below 200 K. In general, for a magnetic system $S_{zz}$ should decrease with the magnetic field. The unconventional positive behavior of the thermopower with field has been previously reported in a MnGe [40] system as well, where the authors relate the increase in $S_{zz}$ to the enhanced magnetic fluctuations at the phase boundary resulting in the energy dependence of the transport lifetime. In the case of MnGe, a positive magnetoresistance (MR) was also reported alongside $S_{zz}$. However, in $ScMn_6Sn_6$, MR shows an almost negligible positive signal with the increase in $\mu_0 H$ (see Fig. S3 [35]). The response of MR and $\Delta S_{zz}/S_{zz}(0)$ to magnetic field is opposite within the TCS phase below $T = 200$ K. This anticorrelation between MR and Seebeck thermopower was also seen in the magnetic topological insulator $MnBi_2Te_4$ [43]. In the present case, we believe that there is some scattering phenomenon within the TCS phase that allows the carriers to gain high entropy values resulting in positive $\Delta S_{zz}/S_{zz}(0)$. Since the enhancement of the signal appears below 200 K, it further suggests that the reduction in thermal fluctuations has a major role to play. Nevertheless, this scattering process is not detectable in the electrical and thermal resistivity. A further theoretical investigation is necessary to identify the exact mechanism behind the $\Delta S_{zz}/S_{zz}(0)$ vs $\mu_0 H$ trend.

Next, we examine the field dependence of the transverse component of the thermal and thermoelectric signal. Magnetic-field-dependent thermal Hall resistivities ($\lambda_{yz}$) and Nernst coefficients ($S_{yz}$) for $\mu_0 H = 9$ to $-9$ T measured at several temperatures are shown in Figs. 4(a) and 4(b), respectively. For clarity, each $\lambda_{yz}$ and $S_{yz}$ curve has been shifted with a certain constant value along the $\lambda_{yz}/S_{yz}$ axis. In Fig. 4(a)

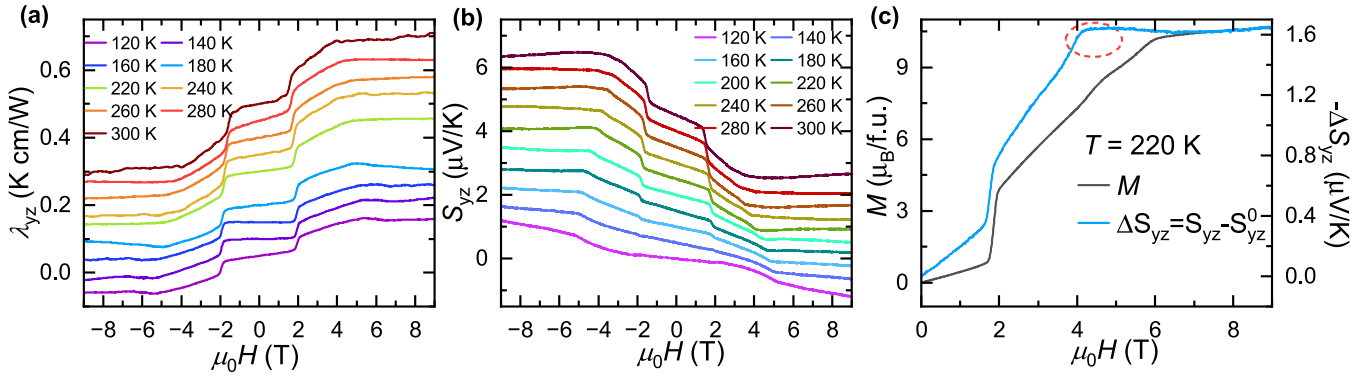


FIG. 4. Magnetic-field-dependent thermal Hall resistivities ($\lambda_{yz}$) and Nernst coefficients ($S_{yz}$) for various temperatures are shown in (a) and (b), respectively. The coefficient $yz$ indicates the applied temperature gradient, $-\Delta T \,||\, z$ axis, and the measured transverse $\Delta T$/thermoelectric voltage $||$ $y$ axis. (c) Comparison between the magnetization curve and residual Nernst coefficient at $T = 220$ K is shown. A residual Nernst coefficient is obtained by subtracting the normal Nernst ($\propto H$) from the measured Nernst coefficient.

the observed $\lambda_{yz}$ vs $\mu_0 H$ follows the behavior of the field-dependent magnetization. Similar to $M$ vs $\mu_0 H$, $\lambda_{yz}$ vs $\mu_0 H$ clearly depicts the DS-TCS magnetic phase transition with a sharp jump at $H_{c1}$ at all measured temperatures, and saturation at $\mu_0 H \geqslant H_{c3}$. The resemblance of the thermal Hall resistivity with that of the magnetization curve distinctly indicates the presence of ATHE in $ScMn_6Sn_6$. As mentioned in the Introduction, the observation of anomalous behavior correlates to the BC. Hence the presence of ATHE in $ScMn_6Sn_6$ implies the presence of large BC. ATHE has been previously reported in isostructural ferrimagnetic $TbMn_6Sn_6$ where its occurrence was related to the BC arising from the massive Dirac gaps [33].

The field-dependent Nernst thermopower [Fig. 4(b)], which is experimentally obtained as $S_{yz} = E_y/\nabla_z T$, also shows identical features as the magnetization curve indicating the presence of ANE. The sign of $S_{yz}$ is in agreement with the reports of $YMn_6Sn_6$ and $TbMn_6Sn_6$ [31,32]. To scrutinize the measured Nernst coefficient, we express it in terms of its constituents, $S_{yz} = S^0_{yz} + \Delta S_{yz}$, where $S^0_{yz}$ is the ordinary Nernst signal which is proportional to the applied magnetic field and $\Delta S_{yz}$ is the residual Nernst coefficient. Since $S^0_{yz} \propto H$, the ordinary contribution can be subtracted from the measured signal by performing the linear fit using the high magnetic field data. After reduction of the normal component from $S_{yz}$, we compare the residual signal at $T = 220$ K with the magnetization. Figure 4(c) shows $\Delta S_{yz}$ vs $\mu_0 H$ and $M$ vs $\mu_0 H$ at $T = 220$ K. Although it seems that the $\Delta S_{yz}$ follows $M$ and matches the magnetization curve at high magnetic fields, on closer inspection it is distinct that there are some additional features in $\Delta S_{yz}$ compared to $M$ as indicated by the red-dashed circle in Fig. 4(c). In general, any superimposed component on the transverse signal which does not follow the magnetization behavior is identified as a topological effect.

The Nernst thermopower can further be decomposed into three components, $S_{yz} = S^0_{yz} + S^A_{yz} + S^T_{yz}$, where $S^A_{yz}$ is the anomalous contribution and $S^T_{yz}$ is the topological addition. With the assumption that $S^A_{yz} \propto M$ and $S^0_{yz} \propto H$, $S^T_{yz}$ can be extracted from the measured Nernst thermopower for each temperature. Figures 5(a) and 5(b) report the educed $-S^A_{yz}$ and $S^T_{yz}$ signals with respect to field at various temperatures, respectively. The anomalous Nernst coefficient was estimated by extrapolating the high-field data to the zero-field value [Fig. S4(a) [35]]. The magnitude of $S^A_{yz}$ at $T = 300$ K is 2.21 μV/K, which is very similar to the value reported for $YMn_6Sn_6$ and $TbMn_6Sn_6$ and comparable to the highest value reported for semimetals $Co_2MnGa$ (Table I). In contrast to $YMn_6Sn_6$ [31], the magnitude of $S^A_{yz}$ increases as $T$ is raised from 120 to 300 K [Fig. S4(b) [35]], indicating a significant contribution from the BC at the Fermi level up to the highest measured temperature. Figure 5(b) confirms the occurrence of the topological Nernst effect $S^T_{yz}$ in $ScMn_6Sn_6$ at all measured temperatures. The magnitude of the response is maximum within the TCS magnetic phase of $ScMn_6Sn_6$. The extremes of the TCS phase are shown by the two black-dashed lines (note, the lower and upper boundaries were identified using $T = 300$ K and $T = 120$ K magnetization curves, respectively). The TCS phase in this system is also responsible for the origin of the topological Hall effect as reported by Zhang *et al.* [29]. The authors in the paper corroborate the theory put forward for $YMn_6Sn_6$ [21] which states that the noncollinear TCS phase gives rise to a dynamical nonzero spin chirality resulting in the deflection of conducting charge carriers and hence producing superimposed geometrical effects on the Hall component. As TNE and THE are both present in the TCS phase of $ScMn_6Sn_6$, we believe their emergence is correlated and they should follow the same theory. Nevertheless, TNE in the TCS phase is not revealed in $YMn_6Sn_6$ [31]. Although the two compounds $YMn_6Sn_6$ and $ScMn_6Sn_6$ share similar magnetic structures and electrical transport properties, the absence of TNE in $YMn_6Sn_6$ suggests that there might be some subtle differences in the spin configuration of the TCS

TABLE I. Comparison between the magnitude of the Nernst coefficient at $T = 300$ K.

| Compound | $S^A_{yz}$ | Ref. |
|---|---|---|
| $Co_2MnGa$ | $\sim 6\ \mu V\ K^{-1}$ | [11] |
| $YMn_6Sn_6$ | $\sim 2\ \mu V\ K^{-1}$ | [31] |
| $TbMn_6Sn_6$ | $2.2\ \mu V\ K^{-1}$ | [32,33] |
| $ScMn_6Sn_6$ | $2.21\ \mu V\ K^{-1}$ | This work |

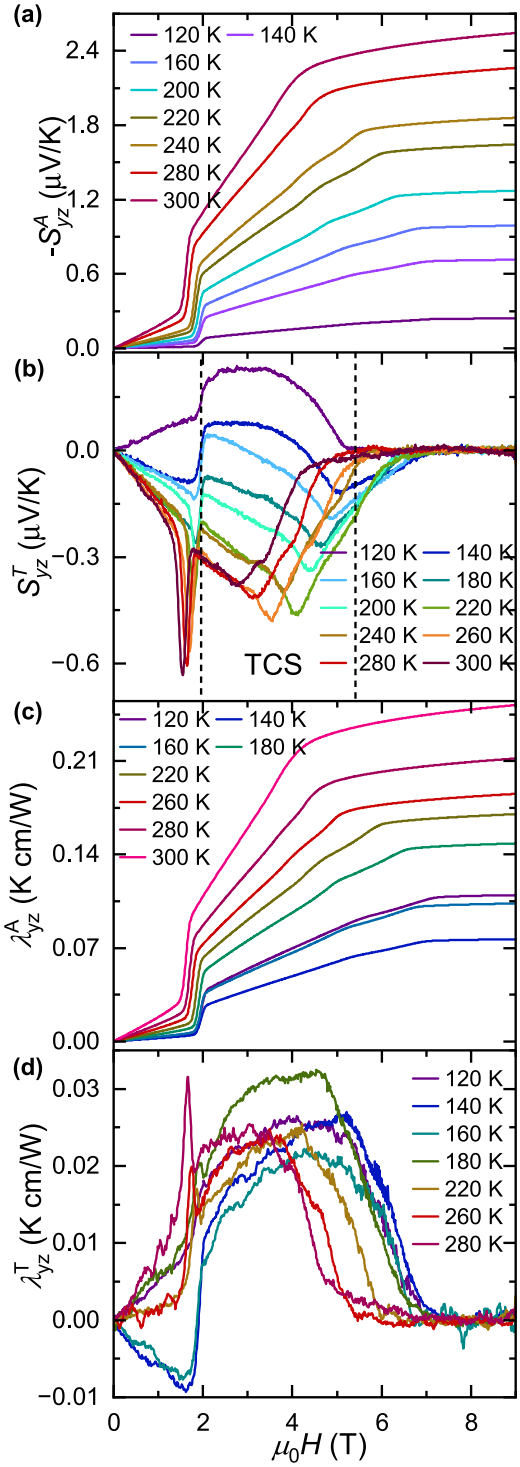


FIG. 5. Anomalous and topological effects. (a) Anomalous Nernst response ($\propto M$) obtained from the measured Nernst signal is shown as a function of magnetic field for various temperatures. (b) Magnetic field dependence of the Nernst signal after subtracting the ordinary ($\propto H$) and anomalous response ($\propto M$). Field dependence of the anomalous (c) and topological (d) Hall contributions to the total thermal Hall signal at various temperatures.

phase of the two materials which needs further exploration. The peak seen for $\mu_0 H < 2$ T [Fig. 5(b)] is probably due to some mismatch in the critical fields responsible for DS to TCS magnetic crossovers as seen by two completely different measurements, magnetization and thermoelectric transport (Fig. S5 [35]). Furthermore, below $T = 200$ K, $S^T_{yz}$ starts to form a concave downward curvature, and eventually changes direction for $T = 120$ K. This $T = 200$ K coincides with the temperature where $\Delta S_{zz}$ starts to show unconventional behavior [Fig. 3(b)], however, we are unable to establish a common phenomenon for this synchronicity. The change in sign of $S^T_{yz}$ at lower temperature was observed in $Fe_3Sn_2$ as well.

Likewise, if we consider that similar to electrical Hall and Nernst thermopower, the total thermal Hall resistivity $\lambda_{yz}$ can also be written as a sum of normal, anomalous, and topological components, i.e., $\lambda_{yz} = \lambda^0_{yz} + \lambda^A_{yz} + \lambda^T_{yz}$, then we can extract the values of $\lambda^A_{yz}$ and $\lambda^T_{yz}$ by following the procedure followed for $S^A_{yz}$ and $S^T_{yz}$. Here, we assume that at high fields the phonon contribution to $\lambda_{yz}$ is linear in field ($\lambda^0_{yz} \propto H$) and $\lambda^A_{yz} \propto M$. Figures 5(c) and 5(d) show the field-dependent obtained values for $\lambda^A_{yz}$ and $\lambda^T_{yz}$, respectively, at various temperatures. Surprisingly, a significant amount of signal for the topological thermal Hall effect is detected for $T = 120$–$280$ K [Fig. 5(d)]. The magnitude of $\lambda^T_{yz}$ becomes almost negligible at $T = 300$ K (Fig. S6 [35]). Although there have been theoretical predictions for the existence of TTHE in kagome [44] and frustrated antiferromagnets [45], identifying it through experiments has been a great challenge. Experimentally, TTHE has been previously reported in a skyrmion lattice system $GaV_4Se_8$ [14], a magnetic insulator, below 15 K. It is theoretically predicted that the motion of the noncollinear spin textures and magnons are coupled in the presence of a fictitious electromechanical potential [46,47]. Since the maxima of $\lambda^T_{yz}$ are also limited to the TCS phase, this makes us suspect that in $ScMn_6Sn_6$, the nonzero spin chirality in the TCS phase also deflects the quasiparticlelike magnons which carry thermal currents along with electrons, resulting in $\lambda^T_{yz}$. The exact mechanism responsible for generating TTHE in $ScMn_6Sn_6$ is to be explored in the future.

To get deeper insight about the origin of the anomalous behavior in $ScMn_6Sn_6$ we compare the temperature evolution of coefficients obtained from three independent measurements, electrical, thermal, and thermoelectric, at 7 T, the regime of the saturated magnetic state. Figure 6(a) shows the temperature progression of $\lambda^A_{yz}$, $-S^A_{yz}$, and $\rho^A_{yz}$ at 7 T. Each of these quantities has been normalized to itself to see the trend more clearly. Although these transverse coefficients $\lambda^A_{yz}$, $-S^A_{yz}$, and $\rho^A_{yz}$ have been acquired separately from thermoelectric, thermal, and electrical measurements, respectively, their response to increasing temperature remains the same. The magnitude of all three increases with temperature values from $T = 120$ to 300 K; this similarity between the coefficients indicates that these effects have a common origin, the BC of $ScMn_6Sn_6$.

Lastly, we define the transverse component of the thermoelectric tensor, $\alpha_{yz}$, which allows us to correlate the electrical and thermoelectric transport properties. For thermoelectric measurements, the electrical current flowing through the ma-

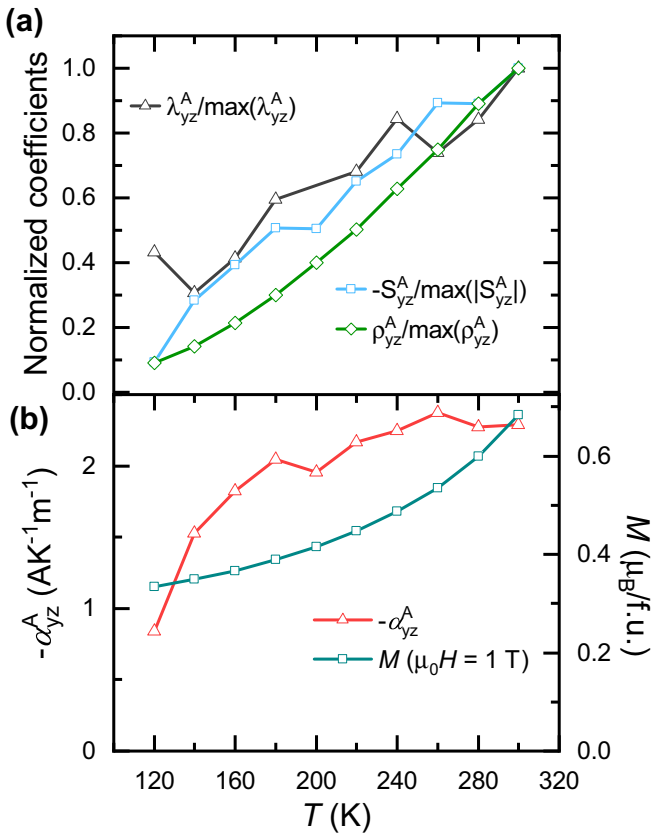


FIG. 6. (a) Temperature evolution of the various normalized coefficients: $\lambda^A_{yz}$, $-S^A_{yz}$, and $\rho^A_{yz}$ at 7 T. (b) Thermal dependence of the anomalous thermoelectric linear response tensor ($\alpha^A_{yz}$) and magnetization at 1 T.

terial is zero. In such a situation $\alpha_{yz}$ can be defined as [11,12,48]

$$\alpha_{yz} = (S_{yz}\sigma_{zz} + S_{zz}\sigma_{yz}). \tag{6}$$

In terms of electrical resistivity the above equation can be rewritten as

$$\alpha_{yz} = \frac{S_{yz}\rho_{zz} - S_{zz}\rho_{yz}}{\rho_{zz}\rho_{yy} + \rho^2_{yz}}, \tag{7}$$

such that $\alpha^A_{yz} = \frac{S^A_{yz}\rho_{zz} - S_{zz}\rho^A_{yz}}{\rho_{zz}\rho_{yy} + \rho^2_{yz}}$. Figure 6(b) displays the temperature profile of the anomalous coefficient of the thermoelectric tensor $-\alpha^A_{yz}$ and compares it with the magnetization ($M$) at $\mu_0 H = 1$ T. $\alpha^A_{yz}$ is obtained by extrapolating the slope of high-field data to the zero-field value (Fig. S7 [35]). For a conventional ferromagnetic system, it is required that $\alpha^A_{yz}$ scales with the temperature dependence of the magnetization [11,49]. In the present case, $\alpha^A_{yz}$ and $M$ do not scale linearly, however, similar to $M$ the magnitude of $\alpha^A_{yz}$ increases with the temperature. Moreover, $\alpha^A_{yz}$ vs $T$ of $ScMn_6Sn_6$ does not follow the behavior of $\alpha^A_{yz}$ vs $T$ of $YMn_6Sn_6$ [31]. In $YMn_6Sn_6$ the magnitude of $\alpha^A_{yz}$ lowers with higher temperature. We do not have a clear understanding about the differences in the thermal dependence of $\alpha^A_{yz}$ in these isostructural compounds. [Note: The magnitudes of the error bars obtained from the fitting for the physical quantities ($\lambda^A_{yz}$, $S^A_{yz}$, $\rho^A_{yz}$, and $\alpha^A_{yz}$) reported in Fig. 6 are in the order of $10^{-5}$–$10^{-6}$.]

## IV. CONCLUSION

In conclusion, we explored the thermal and thermoelectric properties of $ScMn_6Sn_6$. It displays a thermal Hall effect and Nernst thermopower with a magnitude of 2.21 μV/K anomalous Nernst signal at $T = 300$ K. A field-dependent study on $ScMn_6Sn_6$ demonstrates the presence of an unconventional Seebeck thermopower behavior below $T = 200$ K, which is not usually observed in magnetic materials. Most importantly, we revealed that this material not just exhibits a topological Hall effect [29], but also topological Nernst and topological thermal Hall effects in the transverse conical spiral magnetic phase. Both these effects are extremely difficult phenomena to discern. This makes $ScMn_6Sn_6$ a unique and rare example of a skyrmion-free system which manifests all three topological effects: electrical, thermal, and thermoelectric. This study opens up the possibility to explore these effects in different materials with chiral spin fluctuations via thermal and thermoelectric measurement techniques.

## ACKNOWLEDGMENTS

R.P.M., S.M., and D.G.M. acknowledge the support from AFOSR MURI (Novel Light-Matter Interactions in Topologically Non-Trivial Weyl Semimetal Structures and Systems), Grant No. FA9550-20-1-0322. W.R.M., S.D., R.X., and T.M. acknowledge support from the Gordon and Betty Moore Foundation's EPiQS Initiative, Grant No. GBMF9069 to D.G.M. H.Z. acknowledges support from the U.S. Department of Energy, Office of Science, Basic Energy Sciences, Materials Sciences and Engineering Division.

[1] M. Ikhlas, T. Tomita, T. Koretsune, M.-T. Suzuki, D. Nishio-Hamane, R. Arita, Y. Otani, and S. Nakatsuji, Nat. Phys. **13**, 1085 (2017).
[2] K. K. Kolincio, M. Hirschberger, J. Masell, S. Gao, A. Kikkawa, Y. Taguchi, T.-h. Arima, N. Nagaosa, and Y. Tokura, Proc. Natl. Acad. Sci. USA **118**, e2023588118 (2021).
[3] C. Wuttke, F. Caglieris, S. Sykora, F. Scaravaggi, A. U. B. Wolter, K. Manna, V. Süss, C. Shekhar, C. Felser, B. Büchner, and C. Hess, Phys. Rev. B **100**, 085111 (2019).
[4] S. Guo, Y. Xu, R. Cheng, J. Zhou, and X. Chen, Innovation **3**, 100290 (2022).
[5] M.-E. Boulanger, G. Grissonnanche, S. Badoux, A. Allaire, É. Lefrançois, A. Legros, A. Gourgout, M. Dion, C. Wang, X. Chen *et al.*, Nat. Commun. **11**, 5325 (2020).
[6] T. Ideue, T. Kurumaji, S. Ishiwata, and Y. Tokura, Nat. Mater. **16**, 797 (2017).
[7] T. Saito, K. Misaki, H. Ishizuka, and N. Nagaosa, Phys. Rev. Lett. **123**, 255901 (2019).

[8] H. Zhang, C. Q. Xu, and X. Ke, Phys. Rev. B **103**, L201101 (2021).

[9] N. Nagaosa, J. Sinova, S. Onoda, A. H. MacDonald, and N. P. Ong, Rev. Mod. Phys. **82**, 1539 (2010).

[10] T. Asaba, V. Ivanov, S. Thomas, S. Savrasov, J. Thompson, E. Bauer, and F. Ronning, Sci. Adv. **7**, eabf1467 (2021).

[11] S. N. Guin, K. Manna, J. Noky, S. J. Watzman, C. Fu, N. Kumar, W. Schnelle, C. Shekhar, Y. Sun, J. Gooth *et al.*, NPG Asia Mater. **11**, 16 (2019).

[12] T. Liang, J. Lin, Q. Gibson, T. Gao, M. Hirschberger, M. Liu, R. J. Cava, and N. P. Ong, Phys. Rev. Lett. **118**, 136601 (2017).

[13] A. Neubauer, C. Pfleiderer, B. Binz, A. Rosch, R. Ritz, P. G. Niklowitz, and P. Böni, Phys. Rev. Lett. **102**, 186602 (2009).

[14] M. Akazawa, H.-Y. Lee, H. Takeda, Y. Fujima, Y. Tokunaga, T.-h. Arima, J. H. Han, and M. Yamashita, Phys. Rev. Res. **4**, 043085 (2022).

[15] M. Nakamura, D. Morikawa, X. Yu, F. Kagawa, T.-h. Arima, Y. Tokura, and M. Kawasaki, J. Phys. Soc. Jpn. **87**, 074704 (2018).

[16] T. Kurumaji, T. Nakajima, M. Hirschberger, A. Kikkawa, Y. Yamasaki, H. Sagayama, H. Nakao, Y. Taguchi, T.-h. Arima, and Y. Tokura, Science **365**, 914 (2019).

[17] Y. Shiomi, N. Kanazawa, K. Shibata, Y. Onose, and Y. Tokura, Phys. Rev. B **88**, 064409 (2013).

[18] M. Hirschberger, L. Spitz, T. Nomoto, T. Kurumaji, S. Gao, J. Masell, T. Nakajima, A. Kikkawa, Y. Yamasaki, H. Sagayama, H. Nakao, Y. Taguchi, R. Arita, T.-h. Arima, and Y. Tokura, Phys. Rev. Lett. **125**, 076602 (2020).

[19] Y. Xu, L. Das, J. Z. Ma, C. J. Yi, S. M. Nie, Y. G. Shi, A. Tiwari, S. S. Tsirkin, T. Neupert, M. Medarde, M. Shi, J. Chang, and T. Shang, Phys. Rev. Lett. **126**, 076602 (2021).

[20] M. Li, Q. Wang, G. Wang, Z. Yuan, W. Song, R. Lou, Z. Liu, Y. Huang, Z. Liu, H. Lei *et al.*, Nat. Commun. **12**, 3129 (2021).

[21] N. J. Ghimire, R. L. Dally, L. Poudel, D. C. Jones, D. Michel, N. T. Magar, M. Bleuel, M. A. McGuire, J. S. Jiang, J. F. Mitchell, J. W. Lynn, and I. I. Mazin, Sci. Adv. **6**, eabe2680 (2020).

[22] J.-X. Yin, W. Ma, T. A. Cochran, X. Xu, S. S. Zhang, H.-J. Tien, N. Shumiya, G. Cheng, K. Jiang, B. Lian *et al.*, Nature (London) **583**, 533 (2020).

[23] S. Peng, Y. Han, G. Pokharel, J. Shen, Z. Li, M. Hashimoto, D. Lu, B. R. Ortiz, Y. Luo, H. Li, M. Guo, B. Wang, S. Cui, Z. Sun, Z. Qiao, S. D. Wilson, and J. He, Phys. Rev. Lett. **127**, 266401 (2021).

[24] H. W. S. Arachchige, W. R. Meier, M. Marshall, T. Matsuoka, R. Xue, M. A. McGuire, R. P. Hermann, H. Cao, and D. Mandrus, Phys. Rev. Lett. **129**, 216402 (2022).

[25] W. Ma, X. Xu, J.-X. Yin, H. Yang, H. Zhou, Z.-J. Cheng, Y. Huang, Z. Qu, F. Wang, M. Z. Hasan, and S. Jia, Phys. Rev. Lett. **126**, 246602 (2021).

[26] S. Mozaffari, W. R. Meier, R. P. Madhogaria, S.-H. Kang, J. W. Villanova, H. W. S. Arachchige, G. Zheng, Y. Zhu, K.-W. Chen, K. Jenkins, D. Zhang, A. Chan, L. Li, M. Yoon, Y. Zhang, and D. G. Mandrus, arXiv:2305.02393.

[27] W. R. Meier, R. P. Madhogaria, S. Mozaffari, M. Marshall, D. E. Graf, M. A. McGuire, H. W. S. Arachchige, C. L. Allen, J. Driver, H. Cao, and D. Mandrus, arXiv:2306.07868.

[28] G. Pokharel, S. M. L. Teicher, B. R. Ortiz, P. M. Sarte, G. Wu, S. Peng, J. He, R. Seshadri, and S. D. Wilson, Phys. Rev. B **104**, 235139 (2021).

[29] H. Zhang, C. Liu, Y. Zhang, Z. Hou, X. Fu, X. Zhang, X. Gao, and J. Liu, Appl. Phys. Lett. **121**, 202401 (2022).

[30] Q. Wang, K. J. Neubauer, C. Duan, Q. Yin, S. Fujitsu, H. Hosono, F. Ye, R. Zhang, S. Chi, K. Krycka, H. Lei, and P. Dai, Phys. Rev. B **103**, 014416 (2021).

[31] S. Roychowdhury, A. M. Ochs, S. N. Guin, K. Samanta, J. Noky, C. Shekhar, M. G. Vergniory, J. E. Goldberger, and C. Felser, Adv. Mater. **34**, 2201350 (2022).

[32] X. Xu, J.-X. Yin, W. Ma, H.-J. Tien, X.-B. Qiang, P. S. Reddy, H. Zhou, J. Shen, H.-Z. Lu, T.-R. Chang *et al.*, Nat. Commun. **13**, 1197 (2022).

[33] H. Zhang, J. Koo, C. Xu, M. Sretenovic, B. Yan, and X. Ke, Nat. Commun. **13**, 1091 (2022).

[34] P. C. Canfield, T. Kong, U. S. Kaluarachchi, and N. H. Jo, Philos. Mag. **96**, 84 (2016).

[35] See Supplemental Material at http://link.aps.org/supplemental/10.1103/PhysRevB.108.125114 for the x-ray pattern, schematic of the measurement setup, electrical resistivity data, extraction of the anomalous coefficients, and decomposition of the Nernst and anomalous thermal Hall signal.

[36] *Thermal Conductivity: Theory, Properties, and Applications*, edited by T. M. Tritt (Kluwer Academic/Plenum, New York, 2004).

[37] N. Ashcroft and N. Mermin, *Solid State Physics* (Saunders College, Philadelphia, 1976).

[38] Y. Onose, Y. Shiomi, and Y. Tokura, Phys. Rev. Lett. **100**, 016601 (2008).

[39] H. B. Callen, Phys. Rev. **73**, 1349 (1948).

[40] Y. Fujishiro, N. Kanazawa, T. Shimojima, A. Nakamura, K. Ishizaka, T. Koretsune, R. Arita, A. Miyake, H. Mitamura, K. Akiba *et al.*, Nat. Commun. **9**, 408 (2018).

[41] G. Mahan, Solid State Phys. **51**, 81 (1979).

[42] Y. Nishino, S. Deguchi, and U. Mizutani, Phys. Rev. B **74**, 115115 (2006).

[43] H. Zhang, C. Q. Xu, S. H. Lee, Z. Q. Mao, and X. Ke, Phys. Rev. B **105**, 184411 (2022).

[44] S. A. Owerre, Phys. Rev. B **95**, 014422 (2017).

[45] Y. Lu, X. Guo, V. Koval, and C. Jia, Phys. Rev. B **99**, 054409 (2019).

[46] K. A. van Hoogdalem, Y. Tserkovnyak, and D. Loss, Phys. Rev. B **87**, 024402 (2013).

[47] J. Iwasaki, A. J. Beekman, and N. Nagaosa, Phys. Rev. B **89**, 064412 (2014).

[48] L. Ding, J. Koo, L. Xu, X. Li, X. Lu, L. Zhao, Q. Wang, Q. Yin, H. Lei, B. Yan, Z. Zhu, and K. Behnia, Phys. Rev. X **9**, 041061 (2019).

[49] T. Miyasato, N. Abe, T. Fujii, A. Asamitsu, S. Onoda, Y. Onose, N. Nagaosa, and Y. Tokura, Phys. Rev. Lett. **99**, 086602 (2007).